Super-Resolution Microscopy Reveals Structural Mechanisms Driving the Nanoarchitecture of a Viral Chromatin Tether

Margaret J. Grant[1], Dean H. Kedes[*1,2,3], and M. Mitchell Smith[*1]

[1]Department of Microbiology, Immunology and Cancer Biology

[2]Department of Medicine, Division of Infectious Diseases and International Health,

University of Virginia, Charlottesville, VA 22908, USA

[3]Lead Contact

*Corresponding author. Email kedes@virginia.edu (D.H.K.); mms7r@virginia.edu (M.M.S.)

Summary

By engaging in a form of molecular piggybacking onto host chromatin, DNA tumor viruses ensure retention and segregation of their circular genomes (episomes) during sequential cell divisions. Despite elegant functional genetic and crystallographic studies, there is little information that addresses the folding and three-dimensional macromolecular structure of these virally encoded tethers in cells, issues critical for understanding persistent infection by these viruses. Here, we have applied direct stochastic optical reconstruction microscopy (dSTORM) to establish the nanoarchitecture of individual tethers within tumor cells latently infected with the oncogenic human pathogen, Kaposi's sarcoma (KS)-associated herpesvirus (KSHV). Each KSHV tether comprises a series of homodimers of the latency-associated nuclear antigen (LANA) that bind with their C-termini to the array of episomal terminal repeats (TRs) and with their N-termini to host chromatin. Super-resolution imaging revealed that individual KSHV tethers possess similar overall dimensions and, in aggregate, fold to occupy the volume of a prolate ellipsoid. Using plasmid constructs with increasing numbers of TR segments, we found that tethers display a polymer power-law scaling behavior with a scaling exponent characteristic of active chromatin. Remarkably, for plasmids containing a minimal two-TR tether, we were also able to determine the size, separation, and relative orientation of two distinct clusters of bound LANA dimers, each corresponding to a single TR. These data have allowed us to generate a data-driven three-dimensional model of the episomal half of the tether. Our findings integrate and extend previously established work in epifluorescence, crystallography, and epigenetics as they relate to the KSHV field and validate the use of dSTORM in the establishing novel structural insights into the physical basis of individual molecular connections linking host and pathogen genomes.

Keywords

KSHV, HHV8, herpesvirus, nucleosome, dSTORM, episome, terminal repeat, LANA, coiled-coil, DNA bending

Introduction

Kaposi's sarcoma-associated herpesvirus (KSHV) is the etiological agent of Kaposi's sarcoma, an inflammatory tumor of the skin and mucous membranes, as well as two B cell tumors, primary effusion lymphoma (PEL) and multicentric Castleman's disease (Cesarman et al., 1995; Chang et al., 1994; Soulier et al., 1995). KSHV infection is marked by long periods of latency when the virus expresses only a small number of essential genes (Dittmer et al., 1998). Among these is ORF73 that encodes LANA (Kedes et al., 1997; Rainbow et al., 1997), a protein of 1162 amino acids with multiple functions, including the tethering of viral episomes to host chromatin. The N-termini of LANA dimers bind to histones H2A/B and to chromatin-associated bromo-domain proteins (Barbera et al., 2006b, 2006a; Hellert et al., 2013; You et al., 2006). The C-termini of three LANA dimers bind cooperatively to three adjacent 20-bp LANA binding sites (LBS 1, 2, and 3) located in each 801-bp TR (Figure 1A) (Ballestas et al., 1999; Garber et al., 2001, 2002; Hellert et al., 2015; Russo et al., 1996). There are an estimated 35 to 45 TRs per viral episome (Lagunoff and Ganem, 1997) and the tethering function is essential for episomal maintenance within dividing cells and, presumably, persistence in patients (Ballestas and Kaye, 2001; Ballestas et al., 1999; Juillard et al., 2016; Komatsu et al., 2004; Ye et al., 2004).

Initial epifluorescence studies identified LANA as nuclear punctae recognized by serum antibodies from KSHV infected patients (Gao et al., 1996; Kedes et al., 1996; Moore et al., 1996; Simpson et al., 1996). Ten years later, Adang et al. used a combination of flow cytometry and

qPCR to demonstrate a direct proportionality between the number of LANA punctae and the amount of viral DNA, leading to the conclusion that each nuclear dot represented a single viral episome (Adang et al., 2006). Previous studies examining these punctae showed association of LANA with mitotic chromosomes at the resolution of epifluorescence microscopy (Ballestas et al., 1999; Cotter and Robertson, 1999). Kelley-Clarke et al. later suggested preferential localization of these LANA punctae to centromeric and telomeric regions on metaphase chromosomes (Kelley-Clarke et al., 2007). Such studies have provided a solid foundation for further inquiry into the nature of this tethering mechanism.

Many fundamental features of full-length tethers in cells have remained elusive due to the resolution constraints of epifluorescence microscopy. While X-ray crystallography has resolved the structures of an N-terminal 23 amino acid LANA peptide bound to nucleosomes, and a C-terminal 139 amino acid peptide in complex with LBS1 (Barbera et al., 2006a; Hellert et al., 2015), questions remain as to the architectural features of a full-length tether. It is unknown how TR chromatin folds and whether this is consistent among tethers, both within and across cell lines. Questions also remain as to how LANA is distributed across the TRs and whether it attains full occupancy on all three LBSs. Finally, it is not clear how all of these elements influence tether folding and the ability to effectively bind to both viral and host genomes. To address these questions, we applied super-resolution microscopy to study KSHV infected cells with the goal of generating architectural data on full-length KSHV tethers.

Results

The Nanoscale Dimensions of LANA Tethers are Uniform and Consistent Across Different Cell Types

We found that dSTORM resolved each epifluorescent LANA dot into a cluster of individual emissions from fluorophore-labeled anti-LANA mAbs (Figure 1B-J). We interpret these emissions as blinks within a Gaussian localization volume from each conjugated dye molecule present at approximately three dye molecules per antibody, up to six antibodies bound per LANA dimer, and up to three LANA dimers per TR. Since all the episomes from the same virus have the same number of TRs (Boulanger et al., 2005; Judde, 2000), and each TR is 801 bp, we reasoned that the polymer architectures revealed by dSTORM should be similarly consistent across multiple instances. We examined 36 individual LANA tethers from BCBL-1 cells (a KSHV-positive PEL line) and 37 from SLKp/Caki-1p cells, a human epithelial line exogenously infected with KSHV derived from BCBL-1 (Grundhoff and Ganem, 2004; Stürzl et al., 2013). We found that while each tether presented a unique shape, their overall dimensions were similar in the two cell lines (Figure 2A and B). To quantify this similarity, we aligned clusters along their three principal axes and calculated their dimensions and radii of gyration, R_g (see Experimental Procedures), shown in Figure 2C and D. The median R_g for tethers in BCBL1 cells was 332 nm, 95% CI [315, 359] and in SLKp cells it was 347 nm, 95% CI [333, 361]. There was no statistical difference between the R_g of BCBL-1 and SLKp tethers ($P = 0.56$, Mood's Median Test). The similarity of these parameters in two different cell types shows that the polymer folding of KSHV LANA tethers is likely to be intrinsic to the viral episome.

Tether Polymer Conformation has the Characteristics of Active Chromatin

We postulated that if the tethers visualized by dSTORM reflect the underlying TR architecture, then their structural parameters should change systematically with different numbers of TR elements. To challenge that hypothesis, we examined synthetic tethers with different numbers of TRs. We co-transfected BJAB cells, a KSHV-negative human B cell line, with two plasmids, one encoding LANA and the other containing 2, 5, 7, or 8 TRs (Figure S1A and B). In addition, we infected BJAB cells with BAC16 virus that we determined contains approximately 20 TRs (Figure S1C and D). Transfection with a LANA-encoding plasmid and a plasmid lacking any functional TR sequence (p0TR) resulted only in diffuse nuclear staining by epifluorescence (Figure S2), consistent with earlier work (Ballestas et al., 1999; Piolot et al., 2001). In contrast, individual tethers in cells harboring plasmids with 2, 8, or 20 TRs showed an increase in size with increasing number of TRs (Figure 3A-C). This increase was accompanied by a corresponding increase in the number of dSTORM fluorophore emissions and, therefore, anti-LANA Ab binding (Figure 3D).

We next tested whether tethers display polymer-like size scaling with increasing TR number. By plotting R_g against the tether DNA length in bp (domain length, L), we found a power-law scaling, $R_g \alpha L^c$, with exponent $c = 0.35 \pm 0.11$ (Figure 3E). In addition to confirming polymer-like scaling behavior of TRs, this exponent also approximated the value of 0.37 ± 0.02 found by Boettiger and co-workers for active chromatin (Boettiger et al., 2016) and is consistent with previous epigenetic findings at TRs in stably KSHV-infected cell lines (Günther and Grundhoff, 2010; Stedman et al., 2004; Sun et al., 2017). We obtained similar results for TR plasmid scaling in COS7 cells (Figure S3). Using this power scaling relationship, we estimated the number of TRs in a single BCBL-1 episome based on its experimentally determined R_g. Our calculated

value of 46 TRs, 95% CI [40, 57], is consistent with earlier gel electrophoretic estimates of approximately 35-45 TRs (Lagunoff and Ganem, 1997). We performed an identical calculation for SLKp cells and estimated 52 TRs per episome, 95% CI [46, 58]. The similarity of these multiple estimates using different approaches argues that the TR-series plasmids provide biologically relevant information on the folding of full-length native KSHV tethers.

Adjacent TRs are Arranged with a Specific Asymmetric Architecture

Closer analysis of the dSTORM emissions from individual p2TR tethers revealed that they frequently gave rise to two distinct, resolvable clusters (Figure 3A) and alignment of the complete set of 28 p2TR data (see Experimental Procedures) reinforced this separation (Figure 4A). Individual clusters were characterized by an R_g = 90 nm, 95% CI [82, 96], which is in agreement with the R_g = 88 nm predicted by extrapolation of the power-law function to a single TR (Figure 3E). Thus, we interpret the two clusters as the signals emanating from two adjacent TRs. We obtained similar results for p2TR dSTORM images acquired in COS7 cells (Figure S4). The p2TR tethers, individually or as an aligned composite, showed striking asymmetry. They comprised flat pairs of prominently elongated ellipsoids whose centroids were spaced apart by 174 nm, 95% CI [152, 185]. Moreover, the long axes of the two clusters intersected to form a 46° angle (Figure 4B), demonstrating a specific differential placement of the individual TRs within the p2TR structure. These parameters provided strong constraints on the underlying folding of the p2TR chromatin tether.

2TR Tether Images are Consistent with a LANA Coiled-Coil Domain

To begin to interpret these tether images at the molecular level, we evaluated the locations of antibody binding to LANA. The antibody LN53 recognizes the tetrapeptide epitope EQEQ (Toptan et al., 2013). This sequence is present 22 times within the canonical LANA protein

sequence spanning 224 residues, and extending as far as residue 922, which is close to the start of the C-terminal DNA binding domain. With approximately 46 terminal repeats per BCBL1 tether, 6 LANA peptides per TR, 3 dye molecules per antibody, and multiple blinks per dye molecule, we anticipated well over 18,000 dSTORM emissions per LANA tether. Surprisingly, we routinely recovered only approximately 2,000 emissions per tether, suggesting only 2 to 3 functional epitopes per LANA peptide. Examination of the primary protein sequence of LANA with Paircoil2 (McDonnell et al., 2006) revealed a segment strongly predicted to form a coiled-coil (Figure S5; P-value < 0.025). This putative coiled-coil region involves the 19 EQEQ epitope sites closest to the C-terminal DNA binding domain and, thus, would be expected to mask these sites from LN53 binding. The presence of 3 epitope sites N-terminal to the coiled-coil domain (Figure 5A) is consistent with our dSTORM emission counts. Furthermore, the positioning of the antibody epitope by a rigid coiled-coil domain is supported by the 2TR images and the separation evident between the two emissions clusters. With these considerations and taking into account the overall predicted secondary structure, including the known axial rise of a coiled coil of 1.46A/amino acid, we predicted that LN53 antibodies would bind to their LANA epitopes approximately 50 nm distal to the LBS DNA. Since the orientations of the antibodies are unknown, we allowed the emissions from the Alexa Fluor® 647 dye molecules to originate from within a sphere of 13 nm radius, that is, approximately the dimension of an antibody molecule (San Paulo and García, 2000; Silverton et al., 1977). Figure 5B illustrates a molecular model of LANA with these features.

Nucleosome Translational Positioning and LANA-Imposed DNA Bending Are Predicted to Direct TR Chromatin Folding

Previous studies using micrococcal nuclease mapping demonstrated the presence of four nucleosomes in tandem within each TR (Stedman et al., 2004), as shown in Figure 6A. We modeled this approximately 700 bp of nucleosome-wrapped terminal repeat chromatin after the crystal structure of a synthetic tetrasome (Schalch et al., 2005) (Figure 6B) because of its similarity to the spacing of the mapped nucleosomes within the TR. We modeled the remaining approximately 101 bp of the TR chromatin as a DNA segment with a roughly 180° bend centered around the LBS sequences, as shown in Figure 6C. A strong binding interface between adjacent LANA dimers is evident in X-ray crystal structures of the C-terminal DNA binding domain of LANA (Domsic et al., 2013; Hellert et al., 2013) and, therefore, we would expect that the occupancy of three LBS sites by LANA dimers would likewise introduce a bend of that magnitude in the TR DNA of the episomal chromatin (Hellert et al., 2015). Because there are 10 bp per turn in B-form DNA, we joined the tetrasome DNA with the bent LBS DNA such that the translational position of the nucleosomes varied over 9 bp relative to the LBS sites, designated phases 1-9 (Figure 6D). This model predicts that the trajectory of the chromatin fiber from one TR to the next is strongly dependent on the position of the TR nucleosomes and the bending of the LBS DNA by LANA dimers.

A Simple Molecular Model Captures Major Properties of 2TR LANA Tethers

We assembled separate TR models with the tetranucleosome translationally positioned at each of the nine consecutive base pairs and then joined pairs of single TR models to produce the complete set of combinatorial 2TR chromatin models (Figure 6E), keeping the repeat length at 801 bp between LBS1 sites. Of the 81 combinations (9 phases for each tetrasome), steric interference, either within their own structures or with the trajectory of connecting DNA,

eliminated 60 models from further consideration (shown in purple in Figure 6E). Figures 6F and G depict examples of a 2TR phase combination without or with steric hindrance, respectively.

Remarkably, the models captured key features of the 2TR dSTORM images. The "phase 8" model, in particular, mimicked features of the combinatorial 2TR image (Figure 7A). The assembly of three LANA dimers with each individual TR of the 2TR model produced an elongated arrangement of epitope binding sites and dye emissions. Furthermore, the long axes of these epitope binding sites give rise to approximately a 45° angle by the combination of tetranucleosome positioning and LBS DNA bending. The distance between the centers of the two sets of epitopes was approximately 151 nm. Both the angle and spacing of emissions in the model approximated those of the experimental dSTORM data (Figure 4).

We tested the ability of our chromatin models to account for the dSTORM data of individual tethers by optimizing the fit of the modeled epitope sites (dye locations) to the experimental p2TR emissions data (see Experimental Procedures). The phase of the tetranucleosome in TR2 is critical for modeling the dSTORM emission data because it is located between the two LBS DNA sequences. While the phase of the tetranucleosome in TR1 is presumably important for the connection to upstream chromatin, its phase does not affect the structural relationship between the LANA dimers in the two TRs. Therefore, we fit each of the 28 p2TR datasets with the 8 chromatin models combining phase 7 for TR1 since it was compatible with each of phases 2-9 for TR2 (Figure 6E). The best fits were then scored by the fraction of dSTORM emissions that intersected with the model-predicted emission volume. One example of such a fit is shown in Figure 7B and Supplementary Video 1. Overall, the median fraction of dSTORM emissions

accounted for by the optimal model was 0.72, 95% CI [0.59, 0.84] (Figure 7C) for the p2TR structures assembled in BJAB cells. We carried out the same analysis of p2TR LANA tethers expressed in COS7 cells and found the median fraction of emissions covered to be 0.78, 95% CI [0.66, 0.94] (Figure S6). Interestingly, we found that the TR2 nucleosome phasing of the model with the optimal fit depended on the particular p2TR LANA tether we examined, with phases 5-9 predominating (Figure S7). This range of phases suggests a basis for the variability seen among the shapes of individual LANA tethers comprised of larger numbers of TRs (Figure 2).

Discussion

Three-dimensional Views of Viral-Chromatin Tethers at Super Resolution

The sub-diffraction, three-dimensional images from this study offer new insights into the architecture of the tethers linking KSHV episomes to human chromatin within intact cells. Until now, LANA tethers have appeared as poorly defined nuclear punctae via epifluorescence microscopy. In contrast, by applying dSTORM to these tethers, we have now been able to resolve each tether into discrete clusters of individual fluorophore emissions. Furthermore, our ability to determine the Cartesian coordinates of each emission to within 10 and 30 nm has provided us with the data to define the position of the underlying LANA-associated epitopes of single tethers at a resolution approximately 20-fold greater than previously possible, while, for the first time, also providing 3rd (z-axis) dimensional information. The quantity and distribution of these emissions have not only generated insights into the overall size and shape of individual LANA tethers within intact, virally infected cells but also permitted us to draw heretofore unknown conclusions about their composition and structure.

Tethers Have Consistent Dimensions Between Cell Types and Exhibit Folding Characteristic of Active Chromatin

The consistency of the shape and emission counts of KSHV tethers argues that the occupancy distribution and density of LANA binding across the TR region is similar among episomes, even in different cell types (suspension or adherent). This is true in native full-length KSHV tethers in cells harboring the same viral strain, as well as in two cell lines (BJAB and COS7) that we transfected with a TR plasmid series. Our discovery that tethers fold like active chromatin in these different cell types is remarkably consistent with previous literature findings examining epigenetic marks, but is perhaps surprising for a structure evolved to provide attachment. It may be that this configuration is simply a consequence of LANA binding to a nucleosome-depleted region. However, TRs have also evolved as DNA replication origins and their active chromatin state may reflect this function as well.

The Asymmetric Arrangement of Two Adjacent TRs Drives a Working Model of a 2TR Tether

The ability of dSTORM to resolve single TR units within 2TR clusters demonstrates that the episomal half of LANA dimers must be well ordered. If LANA dimers radiated randomly from the LBSs or were highly unstructured in their episomal half, we would be unable to separate discrete clusters in the analyses of plasmids containing 2 TRs. During this study, we also noted a markedly reduced quantity of fluorophore emissions from each tether, leading us to realize that the internal repeats of LANA likely comprise a coiled-coil domain that masks all but the three N-terminal most mAb binding sites.

The fluorophore emissions from each 2TR tether were asymmetrically arranged as two elongated ellipsoids with a 46° angle between their long axes. The placement and distribution of emissions in these ellipsoids were consistent with a model with full LANA occupancy on all three LBSs in

each TR. Models with occupancy of only two LBSs per TR did not account well for our observed emissions data quantitatively or positionally, in large part due to the reduced bending of the underlying LBS DNA (data not shown). Additionally, we found an impact in the translational positioning of the nucleosomes for each TR. Moving each tetranucleosome along the nine possible phases of the DNA helix alters the trajectory of the output TR DNA. This, in turn, greatly impacts the relative positions of the LBSs on adjacent TRs and, hence, their associated anti-LANA fluorophore emissions. The emissions predicted by our optimal translational model with full LBS occupancy formed two clusters with an angle of 45° between their long axes, remarkably close to our measured composite 2TR data. This argues that the translational positioning of nucleosomes and the bending of LBS DNA by LANA dimers largely dictate the folding pattern of the KSHV tether. Interestingly, the architecture driven by these two features presents the LANA N-terminal histone binding domains in a way that facilitates exploration of the surrounding environment, promoting their primary function of tethering to host chromatin.

While the model describes most of the 2TR tethers well, it fits a few poorly mainly due to R_g values on the large end of the spectrum. Others have proposed large multi-LANA dimer complexes based on crystallography (Domsic et al., 2013; Hellert et al., 2013, 2015), and it is possible these 2TR exceptions reflect such assemblies. For the majority of the 2TR tethers, however, it is likely that the fixed packing of tetranucleosomes adapted from their crystallographic structure does not reflect the dynamics and the range of conformations adapted by nucleosomes in vivo. We also note that the histones present in the tetranucleosome crystal structure lacked any posttranslational modifications, unlike the KSHV tether histones, which carry active chromatin modifications and are likely less rigidly packed. Relaxation of our

model's tetranucleosome packing would actually improve the fit with a wider range of our 2TR dSTORM data.

The current working model that we have developed captures major features of the KSHV tether, detailing the likely stoichiometry and relative positions of its major molecular components emanating from the TR region of the viral genome. The model also provides a platform for future experimentation that could include determining the nanoarchitecture of tethers with greater numbers of TRs. We anticipate that these efforts would serve to expand our model while providing new information on the degrees of freedom of nucleosome phasing in adjacent TRs and its effects on tether structure. The impact of metaphase on the structure of the LANA tether also merits further study, since it is unclear how chromatin condensation might affect the nanoarchitecture of the tether during this most critical time of episomal and chromosomal segregation. Likewise, examining the tether during lytic reactivation might provide insight into how the tethering mechanism might change during the episome's own replication and at a time when it is most transcriptionally active. Overall, our application of dSTORM to the KSHV LANA tether establishes super-resolution microscopy as a powerful tool with which to explore the nature of the physical connections between host and viral genomes. This approach has broad applicability to a wide variety of persistent viral pathogens, thus, potentially contributing to our ability to target them therapeutically.

Experimental Procedures

Cell Lines. BCBL-1 cells have been in the laboratory of D.H.K. who was a co-author on the study first describing the line (Renne et al., 1996). BJAB cells were a gift from Don Ganem (Novartis Institutes for Biomedical Research) and are described by Menezes et al. (Menezes et al., 1975). SLKp/Caki-1p (Stürzl et al., 2013) cells were a gift from Adam Grundhoff (Heinrich Pette Institute, Leibniz Institute for Experimental Virology, Hamburg, Germany) and Don Ganem and are described by Grundhoff and Ganem (Grundhoff and Ganem, 2004). SLKp cells were selected despite their inclusion in the ICLAC database of commonly misidentified cell lines because of their utility as an epithelial, non-lymphocytic line and their stable infection with BCBL-1-derived virus. iSLK-BAC16 cells were a gift from Rolf Renne (University of Florida, Department of Molecular Genetics and Microbiology) and are described by Brulois et al. (Brulois et al., 2012). COS-7 cells were a gift from Jim Casanova (University of Virginia). BJAB and BCBL-1 cells had typical lymphocyte non-adherent morphology and were CD45 positive by immunofluorescence staining. BCBL-1 cells were syndecan-1 (CD138) positive by immunostaining and flow cytometry (Adang et al., 2006). BCBL-1, SLKp, and iSLK-BAC16 cells were LANA positive by immunofluorescence staining; BJAB cells were LANA negative.

Adherent cell lines were maintained in Dulbecco's modified Eagle's medium (Gibco) supplemented with 10% fetal bovine serum (Gibco). They were harvested from culture dishes with 0.05% trypsin after a wash with 1X phosphate buffered saline. Non-adherent cell lines were maintained in RPMI 1640 (Gibco) supplemented with 10% fetal bovine serum, 20 mM HEPES, 2 mM L-glutamine, 0.05 mM beta-mercaptoethanol, and 200 μg/mL sodium bicarbonate. All experimental conditions for imaging took place in identical media but lacking phenol red. All cell lines were maintained at 37°C in 5% CO_2 and tested negative for mycoplasma.

Plasmids. The pcDNA3-LANA plasmid was a gift from Rolf Renne (University of Florida, Department of Molecular Genetics and Microbiology) and is described by Renne et al. (Renne et al., 2001). The p8TR plasmid is the 8TR-containing Z6 cosmid subcloned into modified pREP9, as described by Ballestas et al. (Ballestas et al., 1999). The plasmid, produced by the lab of Kenneth Kaye (Harvard Medical School), was a gift from Paul Lieberman (The Wistar Institute).

Plasmids containing 0, 2, 5, and 7 terminal repeats were created by transforming DH5α E. coli (Thermo Fisher Scientific) with the p8TR plasmid and screening by PstI restriction endonuclease digestion for colonies that showed recombination within the TR region and gave rise to a lower or higher number of TRs. Insert size was confirmed by gel electrophoresis, as shown in Figure S1A and B. The plasmids isolated from these E. coli were subsequently grown up in SURE E. coli (Agilent Technologies) to preserve fidelity of the new TR number.

Transfections. $10x10^6$ BJAB cells were transfected with 1μg pNTR plasmid + 1μg pcDNA3-LANA plasmid using Amaxa Nucleofector (Lonza) with Solution V on program T-020. Cells were harvested for analysis at 48 hours post-transfection.

Infection of BJABs with BAC16 virus. Infection of BJABs was performed as described by Plaisance-Bonstaff (Plaisance-Bonstaff, 2012). In brief, iSLK-BAC16 cells were seeded at $3x10^5$/mL in a 6-well plate. After 24 hours, they were induced with doxycycline (1 μg/mL) and sodium butyrate (1 mM). 48 hours later, the media was replaced with 3 mLs RPMI containing BJAB cells at a density of $3x10^5$/mL. Four days later, BJABs were removed from the iSLK-

BAC16 cells and cultured for 14 days with hygromycin selection (100 μg/mL) before staining. A separate, identically treated well of iSLK-BAC16 cells without BJABs was cultured for 7 days, at which point all induced iSLK-BAC16s were found to be dead by Trypan blue exclusion.

Antibodies. The anti-LANA antibody LN53 (rat, monoclonal) (Kellam et al., 1999) was conjugated using an Alexa Fluor® 647 succinimidyl ester kit (Thermo Fisher Scientific).

dSTORM Sample Preparation. Cells were fixed in 4% paraformaldehyde for 10 minutes. After a 20-minute rat IgG block at 4μg/mL, Alexa Fluor®-conjugated LN53 antibody was applied at a concentration of 1:400 in BD Perm/Wash (BD Biosciences) and incubated for 40 minutes. Cells were washed in Perm/Wash and DAPI was then applied at 0.5μg/mL for 15 minutes. Coverslips (Cat. #72204-01, Electron Microscopy Sciences) were cleaned with alkaline peroxide. Their centers were masked off and TetraSpeck 0.1μm beads (Thermo Fisher Scientific) were applied to the rest of the surface; these were attached to the slide at 100°C for 30 min. The center masks were removed and the coverslips were coated in poly-L-lysine for 1 hour. The poly-L-lysine solution was aspirated and the coverslips were air-dried overnight. Cells were deposited (Cytospin 2, Shandon) onto the centers of these prepared coverslips for 4 minutes at 500 rpm. Samples for dSTORM analysis were mounted in a solution of 0.22 mg/mL glucose oxidase, 40 μg/mL catalase, 0.14M beta-mercaptoethanol, and 0.55M glucose.

Instrumentation. dSTORM data were collected using custom instrumentation based on an Olympus IX81-ZDC2 inverted microscope (Olympus America Inc., Melville, NY, USA) configured in a standard geometry for localization microscopy (Gould et al., 2009; Hess et al.,

2006). The illumination beam from a 643 nm diode laser (DL-640-100, CrystaLaser, Reno, NV, USA), coupled to a laser clean-up filter (ZET640/20X, Chroma Technology Corp., Rockingham, VT, USA) and a 5X Galilean beam expander (BEO5M, Thorlabs, Inc., Newton, NJ, USA), was focused on the backplane of a 60X, 1.2NA, water-immersion objective (UPSLAPO60XW, Olympus) by means of a f+350 mm lens (Thorlabs) to yield an illumination profile with a $1/e^2$ radius of 34 μm. Ground state depletion and dSTORM readout of Alexa Fluor® 647 dye molecules was achieved with a laser intensity of 1.9 kW/cm^2 as measured at the sample. Single molecule emissions were collected through the same objective using a filter set comprising a dichroic mirror (Di01-R635, Semrock, Rochester, NY, USA) and emission filter (FF01-692/40, Semrock). The image was expanded using f+75 mm and f+150 mm lenses (Thorlabs) arranged as a ~2X telescope and acquired with an EMCCD camera (iXon^{EM} DU-897D-CS0-BV, Andor Technology PLC, South Windsor, CT, USA) to yield an image pixel size of 0.134 μm(Thompson et al., 2002). Astigmatism for axial localization was introduced using a f+1000 mm cylindrical lens (LJ1516RM-A, Thorlabs) placed in the acquisition path (Huang et al., 2008).

dSTORM Data Acquisition. dSTORM images were acquired using a water-immersion objective to minimize axial compression of the data for LANA tethers located far from the coverslip (Hell et al., 1993). Because of the sensitivity of water-immersion lenses to the tilt of the coverslip (Arimoto and Murray, 2004), axial localization was calibrated for each sample by imaging point-source fluorescent beads attached to the same coverslip as the samples being studied. Images of the astigmatic point spread function were acquired every 50 nm in the axial dimension, spanning 2 μm across the focal plane, controlled by a 3-axis nanopositioning stage

(Nano-LPS100, Mad City Labs Inc., Madison, WI, USA). dSTORM images were collected at a frame rate of 32.4 Hz, for a total of 15,000 to 25,000 frames, using an EM gain of 100 and pre-amplifier gain of 5X on the iXon camera. Transmitted light images were collected every 200 frames to provide subsequent correction for lateral drift during analysis, while axial positioning was stabilized by the ZDC2 instrumentation of the microscope. An epifluorescence image of DAPI staining was saved after the dSTORM data acquisition and the few nuclei exhibiting chromosome condensation were excluded from further analysis.

dSTORM Data Processing. dSTORM images were processed using a pipeline of custom python modules, implementing standard single molecule localization algorithms (Gould et al., 2009). In-house software tools utilized numpy (version 1.11.2) and scipy (version 0.18.1) scientific computing libraries (Jones et al., 2001; van der Walt et al., 2011). Candidate dye emissions were identified by size and photon threshold criteria and localized within an 11 x 11 pixel region of interest. Each point spread function (PSF) was evaluated by fitting with a two-dimensional Gaussian ellipse by least squares to estimate parameters for the x and y center coordinates, amplitude, major and minor axes radii, and an offset. The lateral localization precision (lp) was calculated for each emission as described by Thompson et al. (Thompson et al., 2002). For each emission, photon yield was calculated as the product of the Gaussian amplitude and area, while the background pixel noise was estimated as the standard deviation of intensities from the perimeter pixels of the region of interest. The axial location of a molecule was determined using its major and minor axis radii from the 2D Gaussian fit to interrogate the standard curve established from the point source fluorescent beads (DeSantis et al., 2012; Huang et al., 2008) and its axial localization precision was calculated as described by DeSantis et al.

(DeSantis et al., 2012). The transmitted light images obtained through dSTORM acquisition were used to determine lateral image drift using a sub-pixel crosscorrelation algorithm (Guizar-Sicairos et al., 2008) and dSTORM molecule coordinates were corrected by interpolation.

Statistical Treatments. LANA tethers were characterized by their radius of gyration, calculated as the root mean squared vectors of the emissions using the standard representation,

$$R_g^2 = \frac{1}{N}\sum_{i=1}^{N}(r_i - \acute{r})^2$$

where r_i is the location of individual emissions and $\bar{r}$ is the centroid of all the emissions in the tether. The coordinates of $\bar{r}$ were calculated as the average of the coordinates for all emissions weighted by the inverse of their respective lateral and axial localization precision.

We observed that the sample populations of R_g data for tethers could not be assured to be drawn from normal distributions, by D'Agostino and Pearson's test for normality (D'Agostino and Pearson, 1973). Therefore, further summary and comparative statistics were based on nonparametric approaches. The 95% confidence intervals for median estimates were calculated by bootstrap resampling. The R_g sample populations for BCBL-1 and SLKp tethers were accepted as drawn from the same population distribution (Kolmogorov-Smirnov, P-value = 0.248), but the two could not be assumed to present the same variance by the Levene test for equality (P-value = 0.007) (Levene, 1960). Therefore, the similarity of the BCBL-1 and SLKp tethers were evaluated by Mood's Median test (α = 0.05). Power curve analysis by bootstrap resampling of the BCBL-1 (N=36) and SLKp (N=37) populations revealed that, with a statistical power of 0.8, Mood's Median was expected to reject the null hypothesis of equality if the SLKp

tether median R_g values were 38 nm (11%) or more smaller than that of BCBL-1, or 46 nm (14%) or more larger.

LANA Tether Analysis. The software tools used to analyze and visualize the LANA tethers were supported by the additional Python libraries scikit-learn (version 0.17.1) (Pedregosa et al., 2011), statsmodels (version 0.6.1) (Perktold et al., 2017), Geometric Tools (version wm5) (Schneider and Eberly, 2003), matplotlib (version 1.5.3) (Hunter, 2007), and mayavi.mlab (version 4.5.1) (Ramachandran and Varoquaux, 2011). The dSTORM signals for individual LANA tethers were isolated from the data sets and further processed for analysis. The axial localization precision for each emission was re-evaluated by calculating the individual axial position 1000 times using values of the major and minor PSF widths randomly drawn from their respective error distributions. The larger of this Monte Carlo estimate and the original analytical calculation was saved as the working axial localization precision and emissions with values greater than $\pm$ 60 nm were discarded.

To determine aggregate parameters individual LANA tethers were uniformly oriented by geometry-based principle component analysis and aligned at their centers of mass. The dimensions of the aggregate structures along the X, Y, and Z axes were estimated as the coordinates spanning quantile probabilities from 2.5% to 97.5% of the distribution along each axis. Solid 3D representations of tether emissions are depicted by spheres with a radius equal to their median axial localization precision. Similarly, tether images are rendered as Gaussian spots scaled to a width that is twice the median axial localization precision.

Individual 2TR LANA tethers were analyzed further by dividing their emissions into two groups using k-means clustering. The midpoint between the centers of the two clusters was translated to the zero origin and the complete tether was then oriented to place the two cluster centers along the x-axis on either side of the origin. The tether was then rotated about the x-axis to achieve the greatest variance in the y-dimension. Vectors fit through the long dimensions of the two clusters defined a ”V” geometry, and each tether was then reflected horizontally or vertically or both such that the wider separation was oriented towards the positive y-axis and greatest tilt from vertical was oriented towards the positive x-axis. The complete set of 2TR LANA tethers were then superimposed at their origins to evaluate the parameters of the aggregate structure.

Modeling 2TR LANA tethers. The software written to model 2TR LANA tethers utilized additional python modules from the programming libraries Biopython (version 1.68) (Cock et al., 2009; Hamelryck and Manderick, 2003) and PeptideBuilder (version 1.0.1) (Tien et al., 2013), and the application PyMOL (version 1.7.6) (Schrödinger, LLC, 2015).

The X-ray crystal structure of a dimer of LANA C-terminal DNA binding domains in complex with LBS1 DNA suggests that the upstream LANA peptides may enter on either side of the episomal DNA (Hellert et al., 2015) (PDB 4UZB). Therefore, in modeling LANA dimers, we placed the LN53 antibody epitopes on the N-terminal side of a coiled-coil domain which is then connected by a domain of unknown structure to the dimer of C-terminal DNA binding domains. This model is similar to a more general outline proposed previously (Hellert et al., 2015). We modeled domains of unknown structure based on psi and phi angles from their predicted secondary structure. These were done solely to provide plausible constraints on the placement of

the EQEQ epitopes relative to the LBS, and with the exception of the coiled-coil model (Wood et al., 2014) and C-terminal DNA binding domains with known crystal structures, the models are not expected to match actual LANA protein folding.

2TR models were fit to the dSTORM data using a limited memory approximation of the Broyden-Fletcher-Goldfarb-Shanno algorithm for bound constrained minimization (Byrd et al., 1995) as implemented in SciPy. Each of the two clusters of dSTORM emissions for individual tethers was further divided into three clusters by k-means to yield six centroids per tether. To begin optimization, the center of mass of the six average epitope binding sites in the model was aligned with the center of mass of the six cluster centroids of the dSTORM data and the rotational orientation of the model was randomized. Eighteen parameters were then varied to minimize the Euclidean distance between the model epitope sites and their respective dSTORM cluster centers. For fitting, the model was allowed three dimensions of rotation and three dimensions of translation. The six epitope sites in the model were treated as linear vectors of a fixed 51 nm in length originating at the LBS sites and were allowed to rotate freely but constrained to a maximum 45° tilt from perpendicular to the DNA. The best fit for each model was then evaluated for its ability to account for the dSTORM emissions. The Gaussian probability volumes of the dSTORM emissions were scaled by 2.2 times their lateral and axial localization precision. Similarly, the model epitope site probability volumes were scaled by 2.2 times the median axial and lateral localizations of their associated dSTORM emissions. The fit was then scored for the fraction of the dSTORM ellipsoids intersecting with the epitope ellipsoids of the model.

Author Contributions

MJG co-designed and conducted experiments, and contributed to the manuscript; DHK contributed to the conception of the project, co-designed experiments, and contributed to the manuscript; MMS contributed to the conception of the project, co-designed experiments, conducted and analyzed the dSTORM microscopy, and contributed to the manuscript.

Acknowledgements

We thank Barbara Knowles, Samuel Hess, Travis Gould, and Mudalige Gunewardene for an introduction to super-resolution microscopy and advice on instrumentation and Stefan Bekiranov for discussions. This work was supported in part by the University of Virginia Cancer Center P30CA044579 (D.H.K., M.M.S.). D.H.K. acknowledges support of the National Institute of Dental and Craniofacial Research R01DE022291. M.M.S. acknowledges support of the National Institute of General Medical Sciences RC1GM091175 and R01GM116994.

Author Information

The authors declare no competing financial interests. Correspondence and requests for materials should be addressed to D.H.K. (kedes@virginia.edu) and M.M.S. (mms7r@virginia.edu)

References

Adang, L.A., Parsons, C.H., and Kedes, D.H. (2006). Asynchronous Progression through the Lytic Cascade and Variations in Intracellular Viral Loads Revealed by High-Throughput Single-Cell Analysis of Kaposi's Sarcoma-Associated Herpesvirus Infection. J. Virol. *80*, 10073–10082.

Arimoto, R., and Murray, J.M. (2004). A common aberration with water-immersion objective lenses. J. Microsc. *216*, 49–51.

Ballestas, M.E., and Kaye, K.M. (2001). Kaposi's Sarcoma-Associated Herpesvirus Latency-Associated Nuclear Antigen 1 Mediates Episome Persistence through cis-Acting Terminal Repeat (TR) Sequence and Specifically Binds TR DNA. J. Virol. *75*, 3250–3258.

Ballestas, M.E., Chatis, P.A., and Kaye, K.M. (1999). Efficient Persistence of Extrachromosomal KSHV DNA Mediated by Latency-Associated Nuclear Antigen. Science *284*, 641–644.

Barbera, A.J., Chodaparambil, J.V., Kelley-Clarke, B., Luger, K., and Kaye, K.M. (2006b). Kaposi's sarcoma-associated herpesvirus LANA hitches a ride on the chromosome. Cell Cycle *5*, 1048–1052.

Barbera, A.J., Chodaparambil, J.V., Kelley-Clarke, B., Joukov, V., Walter, J.C., Luger, K., and Kaye, K.M. (2006a). The Nucleosomal Surface as a Docking Station for Kaposi's Sarcoma Herpesvirus LANA. Science *311*, 856–861.

Boettiger, A.N., Bintu, B., Moffitt, J.R., Wang, S., Beliveau, B.J., Fudenberg, G., Imakaev, M., Mirny, L.A., Wu, C., and Zhuang, X. (2016). Super-resolution imaging reveals distinct chromatin folding for different epigenetic states. Nature *529*, 418–422.

Boulanger, E., Duprez, R., Delabesse, E., Gabarre, J., Macintyre, E., and Gessain, A. (2005). Mono/oligoclonal pattern of Kaposi Sarcoma-associated herpesvirus (KSHV/HHV-8) episomes in primary effusion lymphoma cells. Int. J. Cancer *115*, 511–518.

Brulois, K.F., Chang, H., Lee, A.S.-Y., Ensser, A., Wong, L.-Y., Toth, Z., Lee, S.H., Lee, H.-R., Myoung, J., Ganem, D., et al. (2012). Construction and Manipulation of a New Kaposi's Sarcoma-Associated Herpesvirus Bacterial Artificial Chromosome Clone. J. Virol. *86*, 9708–9720.

Byrd, R., Lu, P., Nocedal, J., and Zhu, C. (1995). A Limited Memory Algorithm for Bound Constrained Optimization. SIAM J. Sci. Comput. *16*, 1190–1208.

Cesarman, E., Chang, Y., Moore, P.S., Said, J.W., and Knowles, D.M. (1995). Kaposi's Sarcoma–Associated Herpesvirus-Like DNA Sequences in AIDS-Related Body-Cavity–Based Lymphomas. N. Engl. J. Med. *332*, 1186–1191.

Chang, Y., Cesarman, E., Pessin, M., Lee, F., Culpepper, J., Knowles, D., and Moore, P. (1994). Identification of herpesvirus-like DNA sequences in AIDS-associated Kaposi's sarcoma. Science *266*, 1865–1869.

Cock, P.J.A., Antao, T., Chang, J.T., Chapman, B.A., Cox, C.J., Dalke, A., Friedberg, I., Hamelryck, T., Kauff, F., Wilczynski, B., et al. (2009). Biopython: freely available Python tools for computational molecular biology and bioinformatics. Bioinformatics *25*, 1422–1423.

Cotter, M.A., and Robertson, E.S. (1999). The Latency-Associated Nuclear Antigen Tethers the Kaposi's Sarcoma-Associated Herpesvirus Genome to Host Chromosomes in Body Cavity-Based Lymphoma Cells. Virology *264*, 254–264.

D'Agostino, R., and Pearson, E.S. (1973). Tests for departure from normality. Biometrika *60*, 613–622.

DeSantis, M.C., Zareh, S.K., Li, X., Blankenship, R.E., and Wang, Y.M. (2012). Single-image axial localization precision analysis for individual fluorophores. Opt. Express *20*, 3057–3065.

Dittmer, D., Lagunoff, M., Renne, R., Staskus, K., Haase, A., and Ganem, D. (1998). A Cluster of Latently Expressed Genes in Kaposi's Sarcoma-Associated Herpesvirus. J. Virol. *72*, 8309–8315.

Domsic, J.F., Chen, H.-S., Lu, F., Marmorstein, R., and Lieberman, P.M. (2013). Molecular Basis for Oligomeric-DNA Binding and Episome Maintenance by KSHV LANA. PLoS Pathog. *9*, e1003672.

Gao, S.J., Kingsley, L., Li, M., Zheng, W., Parravicini, C., Ziegler, J., Newton, R., Rinaldo, C.R., Saah, A., Phair, J., et al. (1996). KSHV antibodies among Americans, Italians and Ugandans with and without Kaposi's sarcoma. Nat. Med. *2*, 925–928.

Garber, A.C., Shu, M.A., Hu, J., and Renne, R. (2001). DNA Binding and Modulation of Gene Expression by the Latency-Associated Nuclear Antigen of Kaposi's Sarcoma-Associated Herpesvirus. J. Virol. *75*, 7882–7892.

Garber, A.C., Hu, J., and Renne, R. (2002). Latency-associated Nuclear Antigen (LANA) Cooperatively Binds to Two Sites within the Terminal Repeat, and Both Sites Contribute to the Ability of LANA to Suppress Transcription and to Facilitate DNA Replication. J. Biol. Chem. *277*, 27401–27411.

Gould, T.J., Verkhusha, V.V., and Hess, S.T. (2009). Imaging biological structures with fluorescence photoactivation localization microscopy. Nat. Protoc. *4*, 291–308.

Grundhoff, A., and Ganem, D. (2004). Inefficient establishment of KSHV latency suggests an additional role for continued lytic replication in Kaposi sarcoma pathogenesis. J. Clin. Invest. *113*, 124–136.

Guizar-Sicairos, M., Thurman, S.T., and Fienup, J.R. (2008). Efficient subpixel image registration algorithms. Opt. Lett. *33*, 156–158.

Günther, T., and Grundhoff, A. (2010). The Epigenetic Landscape of Latent Kaposi Sarcoma-Associated Herpesvirus Genomes. PLoS Pathog. *6*, e1000935.

Hamelryck, T., and Manderick, B. (2003). PDB file parser and structure class implemented in Python. Bioinformatics *19*, 2308–2310.

Hell, S., Reiner, G., Cremer, C., and Stelzer, E.H.K. (1993). Aberrations in confocal fluorescence microscopy induced by mismatches in refractive index. J. Microsc. *169*, 391–405.

Hellert, J., Weidner-Glunde, M., Krausze, J., Richter, U., Adler, H., Fedorov, R., Pietrek, M., Rückert, J., Ritter, C., Schulz, T.F., et al. (2013). A structural basis for BRD2/4-mediated host chromatin interaction and oligomer assembly of Kaposi sarcoma-associated herpesvirus and murine gammaherpesvirus LANA proteins. PLoS Pathog *9*, e1003640.

Hellert, J., Weidner-Glunde, M., Krausze, J., Lünsdorf, H., Ritter, C., Schulz, T.F., and Lührs, T. (2015). The 3D structure of Kaposi sarcoma herpesvirus LANA C-terminal domain bound to DNA. Proc. Natl. Acad. Sci. *112*, 6694–6699.

Hess, S.T., Girirajan, T.P.K., and Mason, M.D. (2006). Ultra-High Resolution Imaging by Fluorescence Photoactivation Localization Microscopy. Biophys. J. *91*, 4258–4272.

Huang, B., Wang, W., Bates, M., and Zhuang, X. (2008). Three-Dimensional Super-Resolution Imaging by Stochastic Optical Reconstruction Microscopy. Science *319*, 810–813.

Hunter, J.D. (2007). Matplotlib: A 2D Graphics Environment. Comput. Sci. Eng. *9*, 90–95.

Jones, E., Oliphant, T., and Peterson, P. (2001). SciPy: Open source scientific tools for Python.

Judde, J.-G. (2000). Monoclonality or Oligoclonality of Human Herpesvirus 8 Terminal Repeat Sequences in Kaposi's Sarcoma and Other Diseases. J. Natl. Cancer Inst. *92*, 729–736.

Juillard, F., Tan, M., Li, S., and Kaye, K.M. (2016). Kaposi's Sarcoma Herpesvirus Genome Persistence. Front. Microbiol. *7*.

Kedes, D.H., Operskalski, E., Busch, M., Kohn, R., Flood, J., and Ganem, D. (1996). The seroepidemiology of human herpesvirus 8 (Kaposi's sarcoma-associated herpesvirus): distribution of infection in KS risk groups and evidence for sexual transmission. Nat. Med. *2*, 918–924.

Kedes, D.H., Lagunoff, M., Renne, R., and Ganem, D. (1997). Identification of the gene encoding the major latency-associated nuclear antigen of the Kaposi's sarcoma-associated herpesvirus. J. Clin. Invest. *100*, 2606.

Kellam, P., Bourboulia, D., Dupin, N., Shotton, C., Fisher, C., Talbot, S., Boshoff, C., and Weiss, R.A. (1999). Characterization of monoclonal antibodies raised against the latent nuclear antigen of human herpesvirus 8. J. Virol. *73*, 5149–5155.

Kelley-Clarke, B., Ballestas, M.E., Komatsu, T., and Kaye, K.M. (2007). Kaposi's sarcoma herpesvirus C-terminal LANA concentrates at pericentromeric and peri-telomeric regions of a subset of mitotic chromosomes. Virology *357*, 149–157.

Komatsu, T., Ballestas, M.E., Barbera, A.J., Kelley-Clarke, B., and Kaye, K.M. (2004). KSHV LANA1 binds DNA as an oligomer and residues N-terminal to the oligomerization domain are essential for DNA binding, replication, and episome persistence. Virology *319*, 225–236.

Lagunoff, M., and Ganem, D. (1997). The Structure and Coding Organization of the Genomic Termini of Kaposi's Sarcoma-Associated Herpesvirus (Human Herpesvirus 8). Virology *236*, 147–154.

Levene, H. (1960). Robust Tests for Equality of Variances. In Contributions to Probability and Statistics: Essays in Honor of Harold Hotelling, (Palo Alto: Stanford University Press), pp. 278–292.

McDonnell, A.V., Jiang, T., Keating, A.E., and Berger, B. (2006). Paircoil2: improved prediction of coiled coils from sequence. Bioinformatics *22*, 356–358.

Menezes, J., Leibold, W., Klein, G., and Clements, G. (1975). Establishment and characterization of an Epstein-Barr virus (EBC)-negative lymphoblastoid B cell line (BJA-B) from an exceptional, EBV-genome-negative African Burkitt's lymphoma. Biomed. Publiee Pour AAICIG *22*, 276–284.

Moore, P.S., Gao, S.-J., Dominguez, G., Cesarman, E., Lungu, O., Knowles, D.M., Garber, R., Pellett, P.E., McGeoch, D.J., and Chang, Y. (1996). Primary characterization of a herpesvirus agent associated with Kaposi's sarcomae. J. Virol. *70*, 549–558.

Pedregosa, F., Varoquaux, G., Gramfort, A., Michel, V., Thirion, B., Grisel, O., Blondel, M., Prettenhofer, P., Weiss, R., Dubourg, V., et al. (2011). Scikit-learn: Machine Learning in Python. J. Mach. Learn. Res. *12*, 2825–2830.

Perktold, J., Seabold, S., Taylor, J., and statsmodels contributors (2017). Statsmodels.

Piolot, T., Tramier, M., Coppey, M., Nicolas, J.-C., and Marechal, V. (2001). Close but Distinct Regions of Human Herpesvirus 8 Latency-Associated Nuclear Antigen 1 Are Responsible for Nuclear Targeting and Binding to Human Mitotic Chromosomes. J. Virol. *75*, 3948–3959.

Plaisance-Bonstaff, K. (2012). Analysis of Kaposi's Sarcoma-Associated Herpesvirus miRNAs' Role in the Maintenance of Viral Latency. University of Florida.

Rainbow, L., Platt, G.M., Simpson, G.R., Sarid, R., Gao, S.J., Stoiber, H., Herrington, C.S., Moore, P.S., and Schulz, T.F. (1997). The 222- to 234-kilodalton latent nuclear protein (LNA) of Kaposi's sarcoma-associated herpesvirus (human herpesvirus 8) is encoded by orf73 and is a component of the latency-associated nuclear antigen. J. Virol. *71*, 5915–5921.

Ramachandran, P., and Varoquaux, G. (2011). Mayavi: 3D Visualization of Scientific Data. Comput. Sci. Eng. *13*, 40–51.

Renne, R., Zhong, W., Herndier, B., McGrath, M., Abbey, N., Kedes, D., and Ganem, D. (1996). Lytic growth of Kaposi's sarcoma-associated herpesvirus (human herpesvirus 8) in culture. Nat. Med. *2*, 342–346.

Renne, R., Barry, C., Dittmer, D., Compitello, N., Brown, P.O., and Ganem, D. (2001). Modulation of Cellular and Viral Gene Expression by the Latency-Associated Nuclear Antigen of Kaposi's Sarcoma-Associated Herpesvirus. J. Virol. *75*, 458–468.

Russo, J.J., Bohenzky, R.A., Chien, M.-C., Chen, J., Yan, M., Maddalena, D., Parry, J.P., Peruzzi, D., Edelman, I.S., Chang, Y., et al. (1996). Nucleotide sequence of the Kaposi sarcoma-associated herpesvirus (HHV8). Proc. Natl. Acad. Sci. U. S. A. *93*, 14862–14867.

San Paulo, A., and García, R. (2000). High-resolution imaging of antibodies by tapping-mode atomic force microscopy: attractive and repulsive tip-sample interaction regimes. Biophys. J. *78*, 1599–1605.

Schalch, T., Duda, S., Sargent, D.F., and Richmond, T.J. (2005). X-ray structure of a tetranucleosome and its implications for the chromatin fibre. Nature *436*, 138–141.

Schneider, P.J., and Eberly, D.H. (2003). Geometric Tools for Computer Graphics (San Francisco, CA, USA: Morgan Kaufmann).

Schrödinger, LLC (2015). The PyMOL Molecular Graphics System, Version 1.7.

Silverton, E.W., Navia, M.A., and Davies, D.R. (1977). Three-dimensional structure of an intact human immunoglobulin. Proc. Natl. Acad. Sci. U. S. A. *74*, 5140–5144.

Simpson, G.R., Schulz, T.F., Whitby, D., Cook, P.M., Boshoff, C., Rainbow, L., Howard, M.R., Gao, S.J., Bohenzky, R.A., Simmonds, P., et al. (1996). Prevalence of Kaposi's sarcoma associated herpesvirus infection measured by antibodies to recombinant capsid protein and latent immunofluorescence antigen. Lancet Lond. Engl. *348*, 1133–1138.

Soulier, J., Grollet, L., Oksenhendler, E., Cacoub, P., Cazals-Hatem, D., Babinet, P., d'Agay, M.F., Clauvel, J.-P., Raphael, M., Degos, L., et al. (1995). Kaposi's sarcoma-associated herpesvirus-like DNA sequences in multicentric Castleman's disease [see comments]. Blood *86*, 1276–1280.

Stedman, W., Deng, Z., Lu, F., and Lieberman, P.M. (2004). ORC, MCM, and Histone Hyperacetylation at the Kaposi's Sarcoma-Associated Herpesvirus Latent Replication Origin. J. Virol. *78*, 12566–12575.

Stürzl, M., Gaus, D., Dirks, W.G., Ganem, D., and Jochmann, R. (2013). Kaposi's sarcoma-derived cell line SLK is not of endothelial origin, but is a contaminant from a known renal carcinoma cell line. Int. J. Cancer *132*, 1954–1958.

Sun, R., Tan, X., Wang, X., Wang, X., Yang, L., Robertson, E.S., and Lan, K. (2017). Epigenetic Landscape of Kaposi's Sarcoma-Associated Herpesvirus Genome in Classic Kaposi's Sarcoma Tissues. PLOS Pathog. *13*, e1006167.

Thompson, R.E., Larson, D.R., and Webb, W.W. (2002). Precise nanometer localization analysis for individual fluorescent probes. Biophys. J. *82*, 2775–2783.

Tien, M.Z., Sydykova, D.K., Meyer, A.G., and Wilke, C.O. (2013). PeptideBuilder: A simple Python library to generate model peptides. PeerJ *1*, e80.

Toptan, T., Fonseca, L., Kwun, H.J., Chang, Y., and Moore, P.S. (2013). Complex Alternative Cytoplasmic Protein Isoforms of the Kaposi's Sarcoma-Associated Herpesvirus Latency-Associated Nuclear Antigen 1 Generated through Noncanonical Translation Initiation. J. Virol. *87*, 2744–2755.

van der Walt, S., Colbert, S.C., and Varoquaux, G. (2011). The NumPy Array: A Structure for Efficient Numerical Computation. Comput. Sci. Eng. *13*, 22–30.

Wood, C.W., Bruning, M., Ibarra, A.Á., Bartlett, G.J., Thomson, A.R., Sessions, R.B., Brady, R.L., and Woolfson, D.N. (2014). CCBuilder: an interactive web-based tool for building, designing and assessing coiled-coil protein assemblies. Bioinformatics *30*, 3029–3035.

Ye, F.-C., Zhou, F.-C., Yoo, S.M., Xie, J.-P., Browning, P.J., and Gao, S.-J. (2004). Disruption of Kaposi's Sarcoma-Associated Herpesvirus Latent Nuclear Antigen Leads to Abortive Episome Persistence. J. Virol. *78*, 11121–11129.

You, J., Srinivasan, V., Denis, G.V., Harrington, W.J., Ballestas, M.E., Kaye, K.M., and Howley, P.M. (2006). Kaposi's Sarcoma-Associated Herpesvirus Latency-Associated Nuclear Antigen Interacts with Bromodomain Protein Brd4 on Host Mitotic Chromosomes. J. Virol. *80*, 8909–8919.

Figure Legends

Figure 1. dSTORM offers improved image resolution of LANA tethers

(A) Schematic depiction of the anatomy of a KSHV LANA tether. LANA dimers (shown in green) bind via their N termini to histones H2A/B (yellow). The C termini bind with sequence specificity to three LANA binding sites (LBSs) located on each terminal repeat (TR). Red stars represent fluorescent labels on anti-LANA mAbs.

(B) An anti-LANA stained BCBL-1 cell imaged by differential interference contrast microscopy.

(C) The boxed region in (B) viewed by conventional epifluorescence microscopy.

(D) The same field of view in (C) imaged by dSTORM microscopy. (Scale bars for B-D = 2 μm).

(E, G, and I) The three LANA tethers boxed in (C) are enlarged for better visualization.

(F, H, and J) The three LANA tethers boxed in (D) are enlarged for comparison with their paired standard epifluorescence images (E, G, and I). (Scale bars for E-J = 250 nm).

Figure 2. KSHV LANA tethers have consistent dimensions within and between cell types

(A) Three-dimensional projections of three representative LANA tethers from asynchronous BCBL-1 cells. Red spheres depict the Cartesian coordinates of individual photon emissions, with their radii scaled to the median axial localization precision of 30 nm.

(B) Three representative LANA tethers from asynchronous SLKp cells, shown as in (A). (Scale bars for A and B = 250 nm.)

(C) LANA tethers from BCBL-1 cells (N=36) were oriented by principal axes and aligned at their centroids. The compilation is rendered as Gaussian emissions with 30 nm localization precision and presented from three architectural viewpoints, indicated by the X, Y, and Z directional axes. Median dimensions are shown by the bars.

(D) LANA tethers from SLKp cells (N=37) superimposed and rendered as in (C).

Figure 3. LANA tethers show polymer-like scaling as a function of the number of TRs

(A-C) The 3D-projections of representative LANA tethers from a cell transfected with p2TR (A), p8TR (B), or BAC16 with 20 TRs (C) are shown at identical scales as described in Figure 2. (Scale bar for A-C = 250 nm).

(D) The linear relationship between the median number of emissions and the number of TRs per tether is shown for p2TR (N=28), p5TR (N=39), p7TR (N=13), p8TR (N=17), and BAC16 (N=32) (R^2 = 0.99).

(E) The log of median R_g data for the tethers in (D) are shown as a function of the log of the tether DNA lengths (top axis), or the log of the TR number (bottom axis). The regression (solid red line) through tethers with known numbers of TRs (blue circles) was used to calculate the scaling exponent c = 0.35 ± 0.11 (R^2 = 0.88). This curve was extrapolated (dashed red line) to calculate the number of TRs in a BCBL-1 tether (yellow circle), and an SLKp tether (yellow square). Error bars represent 95% CIs. See also Figures S1, S2, and S3.

Figure 4. p2TR tethers show two distinct clusters of LANA Ab that form a 46° angle between their long axes

(A) Compilation of emission data from 28 p2TR tethers; emissions are rendered as in Figure 2. Median dimensions (nm) of the combined data are shown.

(B) Approximately 2X magnified view of the Y-X projection from a demonstrating the 46° angle formed between the two clusters. See also Figure S4.

Figure 5. The structural and functional domains of LANA include a putative coiled-coil

(A) Diagram of the various domains of LANA, including the nucleosome binding domain (purple), LN53 Ab binding sites outside the coiled coil region (red), coiled-coil region (blue), and TR binding domain (orange). LN53 Ab sites C-terminal to the red region were discounted from the TR modeling due to their being buried within the coiled-coil.

(B) Structural rendering of LANA, showing the features and color scheme laid out in (A). See also Figure S5.

Figure 6. Nucleosome translational positioning and LANA-induced DNA bending predict the trajectory of DNA between TRs

(A) Schematic diagram of a single 801-bp TR showing localization of four nucleosomes (purple ovals) and three LBSs (magenta rectangles) on the DNA (blue).

(B) Structure of DNA (blue) wrapping around four nucleosomes (grey), adapted from the tetrasome crystal structure (PDB 1ZBB).

(C) Structure of three LANA dimers (green) binding to the three LBSs (blue) of a single TR, showing the nearly 180 degree DNA bend formed by protein binding.

(D) A DNA-wrapped tetrasome (blue) displaying the rotational effects of the nine theoretically possible nucleosome phases on the position of the LBS-containing DNA fragment emerging from a single TR (numbered 1 through 9).

(E) Chart depicting the combinations of nucleosome phasing for two sequential TRs (TR1 and TR2). The nucleosome phasing results in "disallowed" arrangements (purple squares), wherein the elements face steric hindrance, and "permitted" arrangements (green squares), in which there is no steric hindrance.

(F-G) An example of a "permitted" phasing (TR1 = phase 5, TR2 = phase 8) is shown in (F), in contrast to a "disallowed" phase (TR1 = phase 1, TR 2 = phase 9) presented in (G). Regions of steric hindrance are marked with white arrows.

Figure 7. dSTORM analysis of p2TR tethers is consistent with a model featuring full LBS and nucleosome occupancy on two sequential TRs

(A) Model depicting two TRs (blue), each containing four nucleosomes (grey) and bound by three LANA dimers (green) occupying LBSs (scale bar = 50 nm). Predicted coiled-coil portions of LANA dimers extend outward at approximately right angles to the LBSs. Magenta spheres depict the position of a 13 nm-long anti-LANA mAb. Two white lines represent the best linear fit connecting three LANA dimers for each TR, forming a 45° angle.

(B) Data from one p2TR example aligned with the model in (A). Red ellipsoids depict the probability volume of individual fluorophore emissions, scaled by their lateral and axial localization precision. White ellipsoids depict the model-predicted probability volumes scaled by data-derived localization precision.

(C) Histogram displaying the distribution of the fraction of observed emissions whose localization precision volumes intersect with the model-predicted volume. See also Figure S6 and S7.

Figures

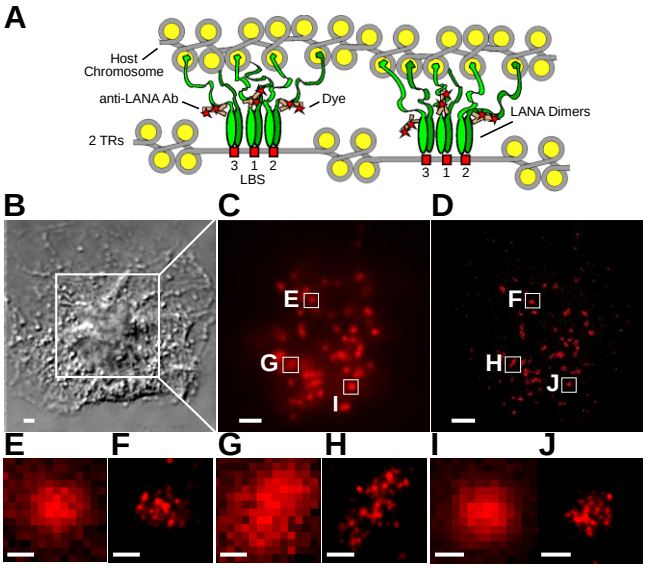
A
Host Chromosome
anti-LANA Ab
Dye
LANA Dimers
2 TRs
3 1 2
LBS
3 1 2
B
C
D
E
F
G
H
I
J
E
F
G
H
I
J

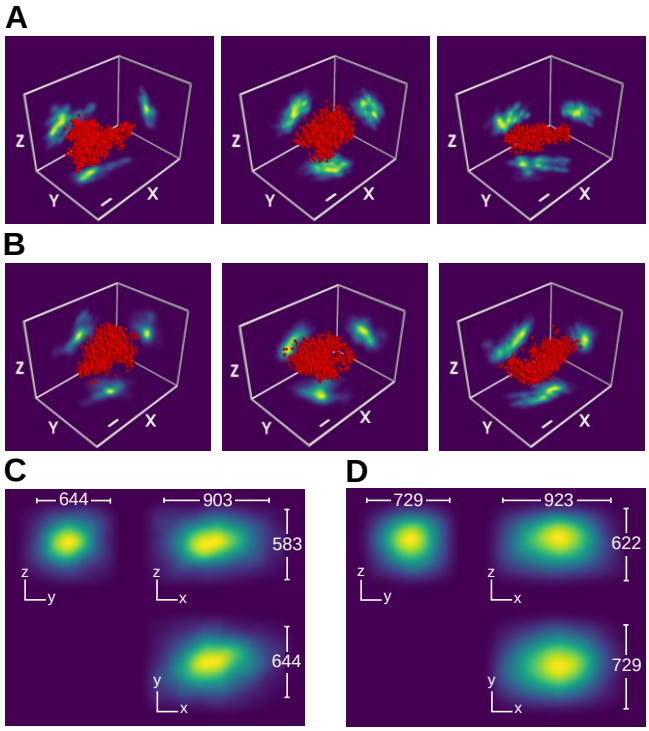
A
B
C
D
Z
Y
X
644
903
583
644
729
923
622
729
z
y
x

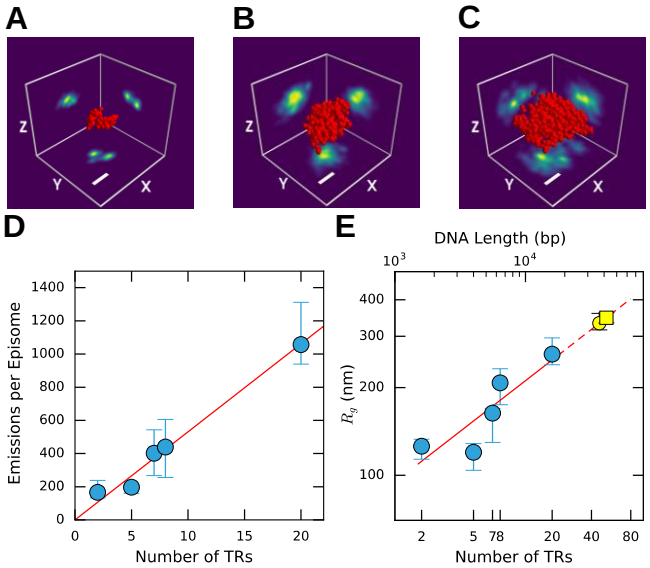
A
B
C
Z
Y
X
D
E
Emissions per Episome
Number of TRs
DNA Length (bp)
R_g (nm)
Number of TRs

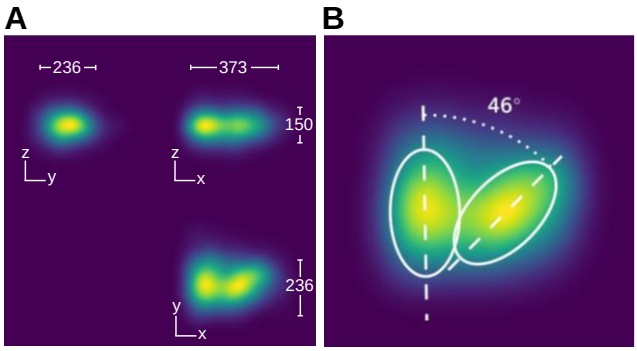
A
B
236
373
150
236
z
y
z
x
y
x
46°

807

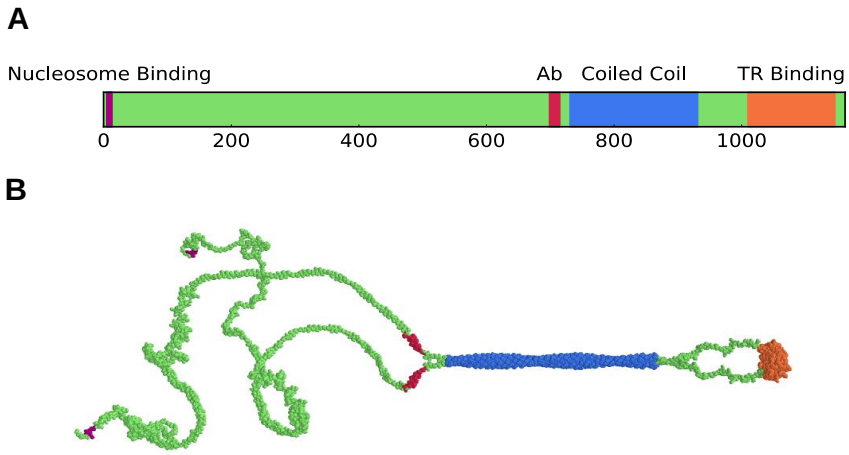
A
Nucleosome Binding
Ab
Coiled Coil
TR Binding
0
200
400
600
800
1000
B

808

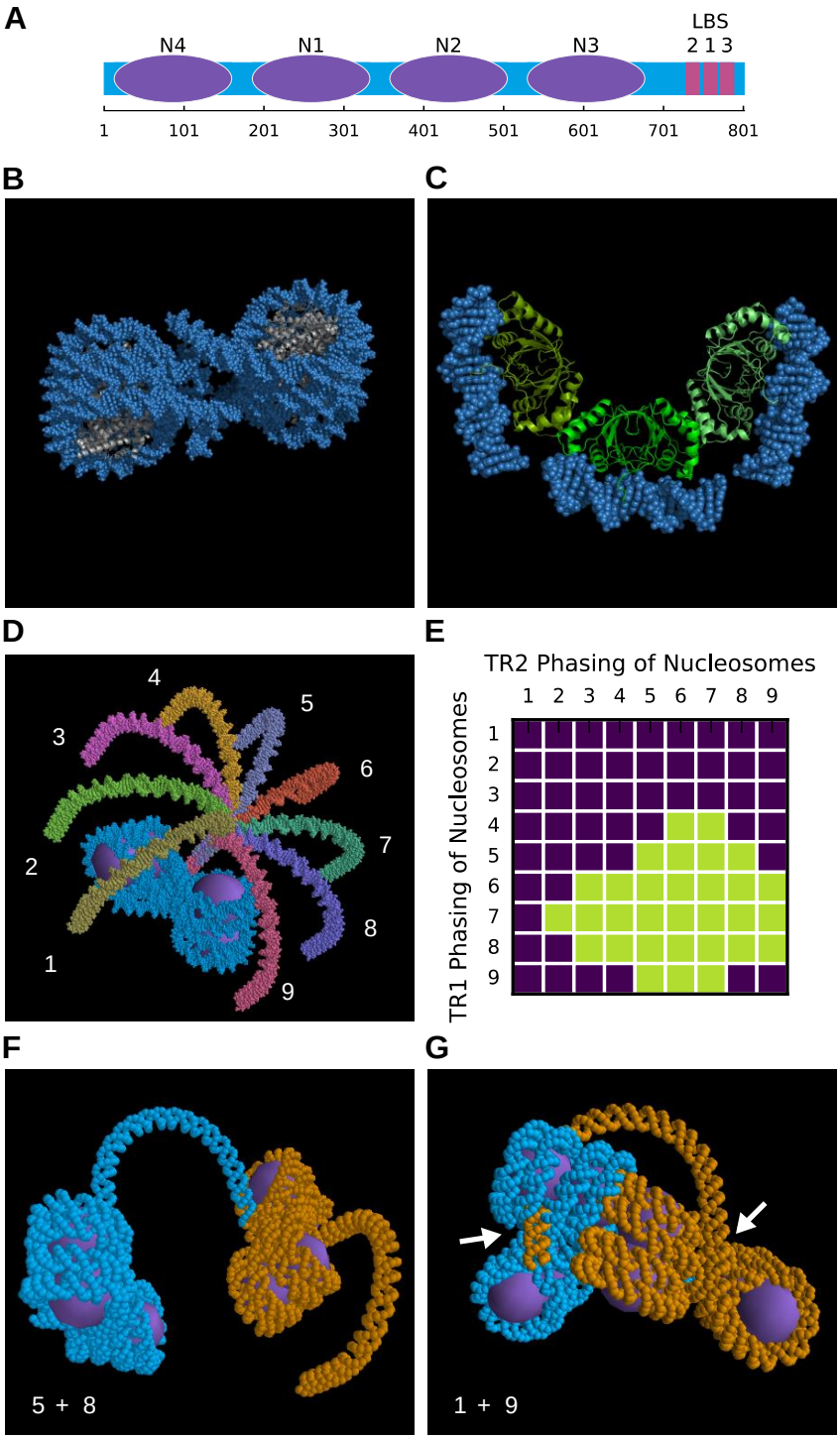
A
N4
N1
N2
N3
LBS
2 1 3
1
101
201
301
401
501
601
701
801
B
C
D
4
5
3
6
7
2
8
1
9
E
TR2 Phasing of Nucleosomes
1 2 3 4 5 6 7 8 9
TR1 Phasing of Nucleosomes
1
2
3
4
5
6
7
8
9
F
5 + 8
G
1 + 9

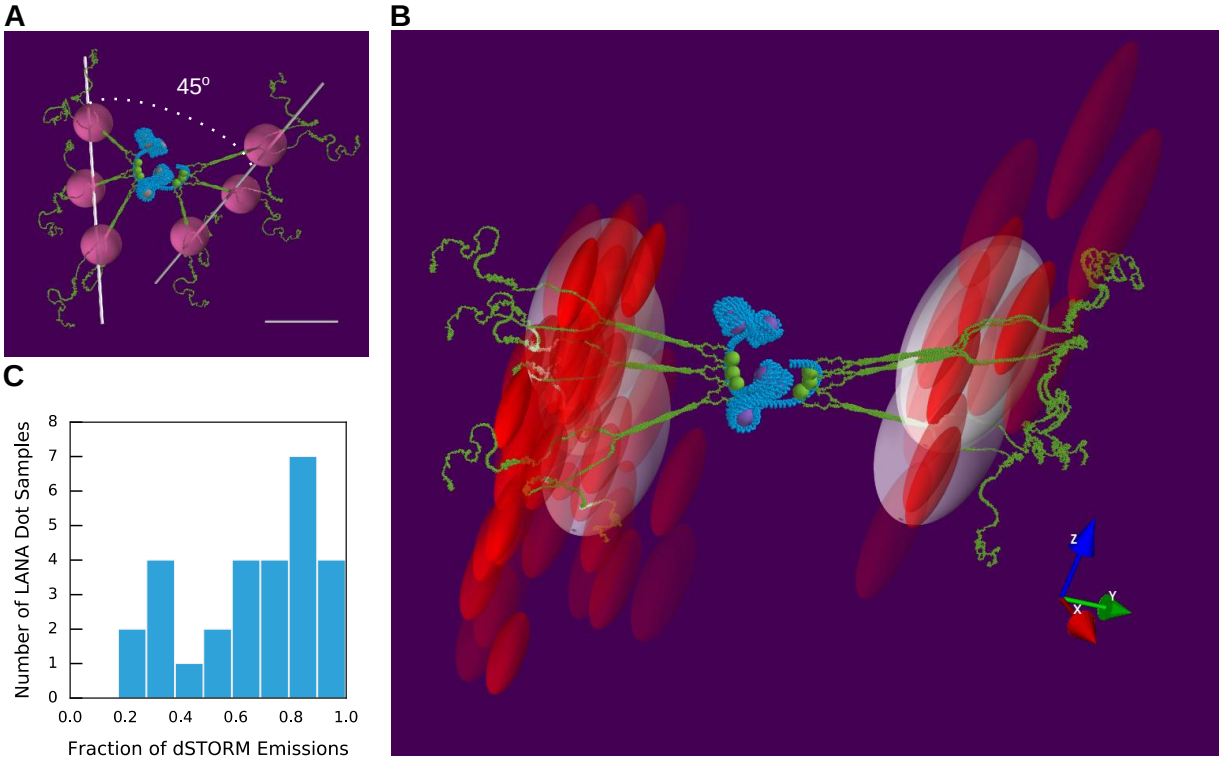
A
45°
B
C
Number of LANA Dot Samples
0
1
2
3
4
5
6
7
8
0.0
0.2
0.4
0.6
0.8
1.0
Fraction of dSTORM Emissions
Z
Y
X